

Article

Weathering Effects on Engineering Geological Properties of Trachydacitic Volcanic Rocks from the Monte Amiata (Southern Tuscany, Italy)

Enrico D'Addario *, Giovanna Giorgetti, Claudia Magrini and Leonardo Disperati * 

Dipartimento di Scienze Fisiche, della Terra e dell'Ambiente, Università degli Studi di Siena, 53100 Siena, Italy; giovanna.giorgetti@unisi.it (G.G.); magrini4@unisi.it (C.M.)

* Correspondence: enrico.daddario@unisi.it (E.D.); disperati@unisi.it (L.D.)

Abstract: Variability in lithology and weathering degree affects physical and mechanical properties of rocks. In this study, we investigated the relationships between weathering degree and engineering geological properties of trachydacitic volcanic rocks from Monte Amiata (central Italy) by coupling field and laboratory analyses. We collected in situ Schmidt hammer tests in the field. We evaluated weathering quantifying the percentage of secondary minerals through thermal analysis in the laboratory. We also determined dry density (ρ_d), specific gravity of solids (G_s), porosity (n) and two-dimensional (2D) porosity as resulted from scanning electron microscopy investigations. The results of our study indicate a negative linear correlation between Schmidt hammer rebound values and secondary mineral percentage. This correlation provides a tool to quantitatively estimate the deterioration of rock uniaxial compressive strength (UCS) as weathering increases. Moreover, thermal analysis turned out to be a quantitative and reproducible method to evaluate weathering degree of magmatic rocks.

Keywords: Schmidt hammer; thermal analysis; weathering; clay minerals; volcanic rock; Monte Amiata



Citation: D'Addario, E.; Giorgetti, G.; Magrini, C.; Disperati, L. Weathering Effects on Engineering Geological Properties of Trachydacitic Volcanic Rocks from the Monte Amiata (Southern Tuscany, Italy). *Geosciences* **2023**, *13*, 299. <https://doi.org/10.3390/geosciences13100299>

Academic Editors: Jesus Martinez-Frias and Dominic E. L. Ong

Received: 11 August 2023

Revised: 22 September 2023

Accepted: 2 October 2023

Published: 6 October 2023



Copyright: © 2023 by the authors. Licensee MDPI, Basel, Switzerland. This article is an open access article distributed under the terms and conditions of the Creative Commons Attribution (CC BY) license (<https://creativecommons.org/licenses/by/4.0/>).

1. Introduction

Variability in lithology and weathering degree affects the physical and mechanical properties of rocks [1–4]. While lithology depends on the rock-forming environment and does not evolve over time, the degree of weathering may be time-dependent, and it may show different degrees of intensity in space. Rock weathering may play an important role on the evolution of landforms [5,6], slope instability [7–13] and engineering geological properties [14–16]. Namely, strength parameters are strictly dependent on both intrinsic lithology and secondary weathering degree [4], the latter being often evaluated through expert-based visual properties [17,18] and/or mineralogical characteristics determined by modal analyses [19]. Indeed, weathering processes change the mineralogy of rocks and, consequently, the mechanical properties which show a negative exponential relationship with altered minerals. A characteristic alteration degree reduces the cohesion of massive lava flows, scoriae and pyroclastites in the Canary Islands, as demonstrated by [20]. In [19], the authors estimated the reduction in shear strength of phonolitic lavas caused by hydrothermal alteration. Even though their sample dataset was quite small, the authors assumed that strength decreases progressively from fresh parent rock to altered material. Reduction in mechanical properties along soil profiles on volcanics and granitoids from Hong Kong have been documented by [21,22]. These authors showed how the shear resistance and normal compression gradient vary along saprolites, from bedrock to surface. Using the 6-fold weathering grade classification scheme of [17], Ref. [23] showed the deterioration of uniaxial compressive strength (UCS) and elastic modulus with increasing weathering grade of granitic rocks.

The mechanical behaviour of different volcanic rocks with respect to alteration, in the volcanic provinces of central and southern Italy have been investigated by [24]. They remarked that the decay of mechanical properties depends on both lithological sample heterogeneity (lava flows, pumices, pyroclastic layers), as well as the degree of alteration. They concluded that the variation in tensile and compressive strength depends upon different grades of alteration for lava and tuffs. As far as pyroclastic deposits are concerned, variation in mechanical parameters depends upon their different textures. As alteration increases, mechanical properties decrease for each tested lithology.

Usually, the effect of weathering processes is estimated by visual interpretation. Most authors refer to the 6-fold classification (G I–G VI) by the International Society for Rock Mechanics (ISRM) Commission [25], based on [17], or to the successive 5-fold classification (W1–W5) adapted by the same ISRM Commission in 1981 [26]. These two methods are defined “quantitative”, even though they are estimated using expert-based judgement of descriptive criteria such as discolouration and discontinuity framework. Attempts at evaluating weathering by means of quantitative approaches may be recognized in the literature. The degree of alteration was established through diffractometric analyses [19]; the authors, however, determined the presence, but not the abundance, of secondary (clay) minerals. Weathering grade determined through visual analysis (W1–W5) was correlated with the decreasing of physico-chemical granitoid properties [27]. Geochemical analyses were performed by [28] to determine the chemical index of alteration (CIA; [29]). The CIA increases with alteration if the tested rock samples share the same initial chemical composition [30,31]. Aydin and Basu [32] and Basu [23] found that rebound values of the Schmidt hammer allowed for the prediction of weathering grades as established from the above-described 6-fold weathering classification scheme. Koken et al. [33] tested physical and mechanical properties of differently weathered granodiorites (from W0 to W3; [26]), and they proposed models to estimate weathering degree for rock engineering geological purposes.

Considering the reviewed literature, we can deduce that mineralogical and petrographic studies are useful for getting direct information on the weathering degree of rocks. However, to date, these approaches have not received enough attention in the engineering geological context where the weathering degree is mainly a matter of qualitative classifications. However, quantifying weathering using reproducible and quantitative methods is tricky; consequently, the role of pervasiveness and intensity of weathering on physical and mechanical parameters of rocks remains the subject of debate and research.

In this framework, we submit a new method for quantifying the weathering degree and related effects on engineering geological properties of volcanic rocks. We focus on Pleistocene trachydacitic volcanic rocks from Monte Amiata (southern Tuscany, Italy) characterized by different weathering degrees. Schmidt hammer rebound measurements are collected in the field, and thermal analyses are performed to quantitatively estimate secondary (clay) mineral content. The correlation between these two parameters allows us to define a new tool to quantitatively estimate the deterioration of rock uniaxial compressive strength (UCS) as weathering increases.

2. Geological Setting

Monte Amiata is a Pleistocene (305–231 ka; [34–36]) volcanic edifice belonging to the Tuscan magmatic province [37], structurally linked to a regional strike-slip fault system [38]. It is composed of trachydacitic and olivine latitic lava flows and domes which have been mapped into different formations [34,39]. Their extension and age are still under debate [36,40,41]. According to [34], the oldest, more extensive, basal trachydacitic complex (BTC) comprises alternating, massive lava flows forming strata of variable thickness. The BTC rocks are porphyritic with glassy to perlitic groundmass. Phenocrysts are plagioclases, sanidine, orthopyroxene, biotite, rare clinopyroxene and resorbed quartz. Following the geological map (Figure 1) modified from [36], the BTC corresponds to the Quaranta Formation (QRT), further divided into two members (QRT1, Marroneto member; and QRT2, Leccio member)

showing a strong compositional homogeneity coupled with textural differences. The Dome and Massive Lava flows Complex (DLC) was emplaced above the BTC, and it is characterized by viscous trachytic to latitic lavas in the form of exogenous domes and short, massive lava flows [34,36]. In the study area, the DLC is represented by the Pianello formation (PNL), particularly the Pianello member (PNL2; Figure 1).

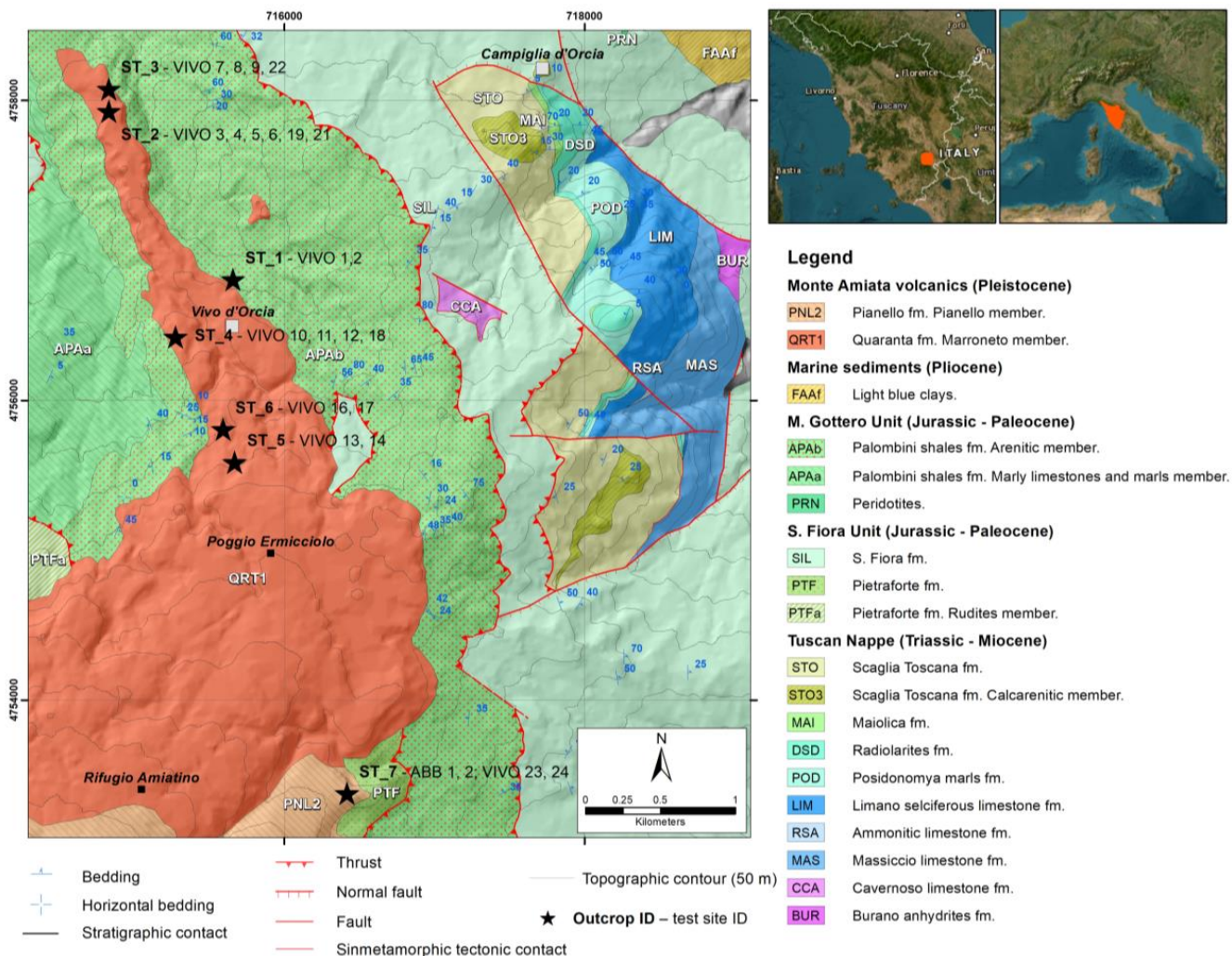


Figure 1. Geological map of the study area with investigated outcrops (**Outcrop ID**—test site ID) (modified after [36]) (coordinate system: EPSG 6707).

The outcrops analysed in this work are shown in Figure 1. They belong to the Marroneto member (QRT1), except for ST₇ which belongs to the Pianello member (PNL2). These rocks mostly consist of trachydacites [36,40] with a fluidal texture marked by the alignment of phenocrysts. Field and petrographic observations allowed us to recognize pumices within QRT1 in an area close to the Vivo d’Orcia village (sports ground, ST₂).

During the field survey, the weathering degree of rocks can first be evaluated based on visual characteristics (Figure 2). Almost unweathered trachydacites and pumices crop out near the Vivo d’Orcia village, while reddish weathered volcanic rocks crop out in the Ermicciolo water spring area. Saprolite *sensu* [42] with different levels of development has been recognized in various locations, with widespread occurrence of corestones.

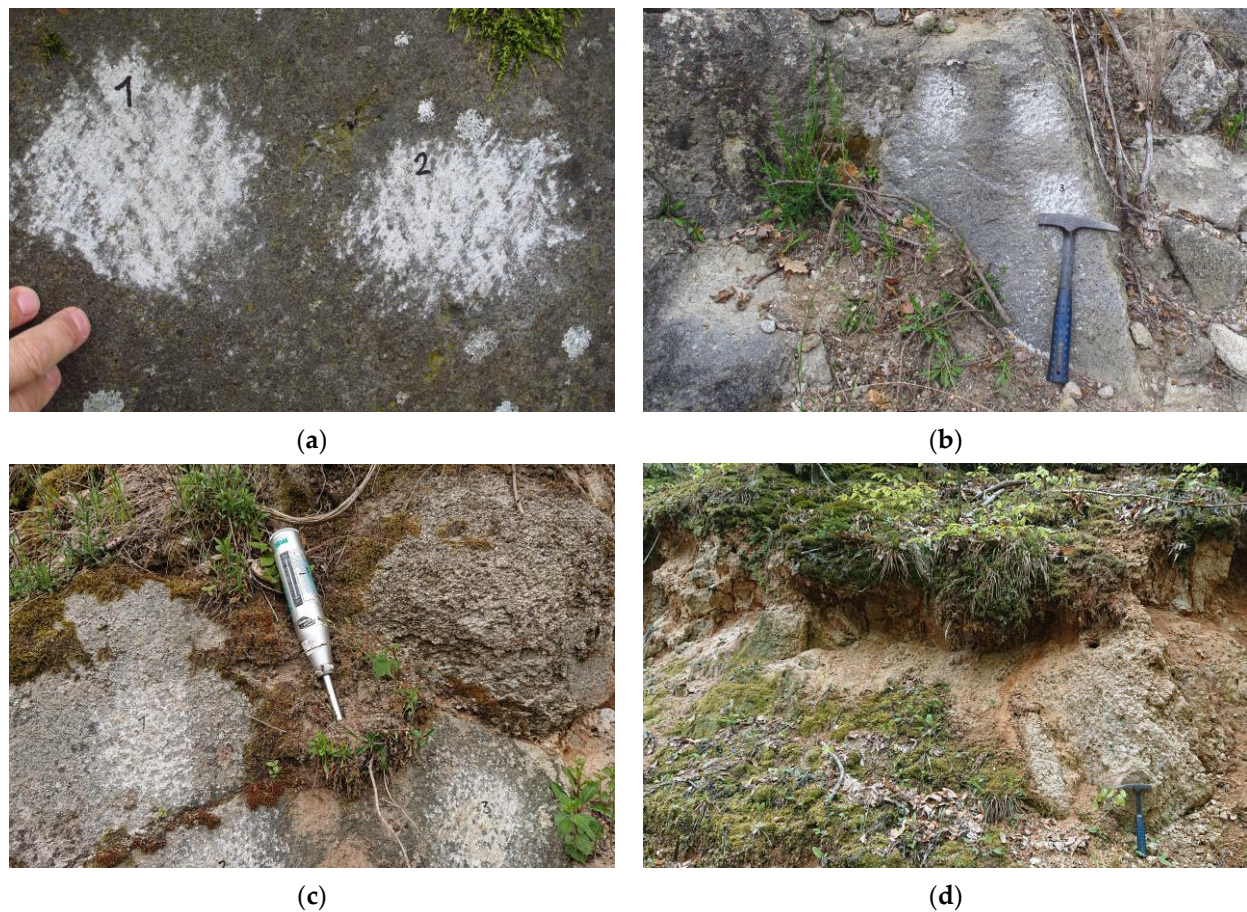


Figure 2. (a) Unweathered trachydacite at ST_1; (b) pumices at ST_2; (c) weathered trachydacite at ST_4; the Schmidt hammer for scale; (d) corestone in saprolite at ST_6; numbers on outcropping rocks identify the measuring surfaces (ms) where we performed the Schmidt hammer tests.

3. Materials and Methods

We focused investigations on outcrops made up of visually unweathered rocks, more precisely from Grade I to Grade III rocks: Ref. [26]. When specified, we performed field measurements and sampling on corestones of zone IIA [43,44].

Samples were collected from the exact same sites where Schmidt measurements were acquired following the recommendation by [32]. In Table 1, sample location, lithology and type of analyses performed are summarized.

With the aim of capturing the effects of local variability of both lithology and weathering conditions, as well as the corresponding engineering geological properties, at least two near-surface (max. ca. 1 m depth) test sites ts were chosen for each selected outcrop. For each test site ts , we collected one or more samples for laboratory tests, while on a subset of the same sites, we also performed Schmidt hammer rebound measurements. The Schmidt hammer has been used in rock mechanics for many decades, as it is regarded as an affordable tool for performing quick and non-destructive tests. The rebound values allow us to estimate mechanical properties of rock, like unconfined compressive strength or modulus of deformation, by using empirical correlations [45–49]. Schmidt hammer measurements for each selected test site ts were carried out within a set of k measuring surfaces ms_k (where $k \cong 3–6$) with dm-scale spacing (Figure 3). Considering the standards proposed in the literature to ensure reliable outputs [26,32,50–53], we chose to perform measurements and to apply the rebound normalization (R_h) according to [53]. Hence, for each test site ts with Schmidt hammer measurements, we obtained a set of ca. 90–120 rebounds, and we calculated the corresponding average rebound value \overline{R}_h .

Table 1. Outcrop and test site (sample) identification (ID), weathering grade [25], lithology descriptions and results of analyses performed in the field and the laboratory; symbols: (-) parameter not determined; (n.d.) parameter not determinable.

Outcrop ID	Test Site ID	Lithology	Weathering Grade	$\rho_d(\text{gr/cm}^3)$	$G_s(-)$	$n(\%)$	$n_{2D}(\%)$	Weight Loss (%)	$\overline{R}_h(-)$
ST_1	VIVO1	trachyte	I	2.41	2.55	5.5	1	1.24	28
ST_1	VIVO2	trachyte	I	2.45	-	-	0.5	0.85	44
ST_2	VIVO3	trachyte	I	2.34	2.51	6.8	10	1.52	23
ST_2	VIVO4	pumice	I	1.60	2.47	35.2	35	2.41	n.d.
ST_2	VIVO5	pumice	I	1.62	-	-	52	2.12	n.d.
ST_2	VIVO6	trachyte	I	2.36	2.52	6.3	2	2.29	38
ST_2	VIVO19	trachyte	I	2.32	2.52	7.6	4	1.30	26
ST_2	VIVO21	pumice	I	1.87	2.51	25.5	20	1.91	19
ST_3	VIVO7	trachyte	I	2.16	2.53	14.6	7	2.72	-
ST_3	VIVO8	trachyte	I	2.45	2.54	3.5	2	1.16	36
ST_3	VIVO9	trachyte	I	2.33	2.51	11.9	3	1.61	-
ST_3	VIVO22	trachyte	I	2.10	2.53	16.7	18	1.85	23
ST_4	VIVO10	trachyte	I	2.35	2.52	6.6	3	1.45	32
ST_4	VIVO11	trachyte	I-II	2.21	2.51	12.0	22	1.87	-
ST_4	VIVO12	trachyte	II	2.13	2.49	14.5	3	2.79	-
ST_4	VIVO18	trachyte	II	2.17	2.43	1.2	3	0.27	-
ST_5	VIVO13	trachyte	II	2.31	2.52	8.2	5	1.31	35
ST_5	VIVO14	trachyte	II	2.31	-	-	5	2.20	-
ST_6	VIVO16	trachyte	III	2.22	2.55	12.6	2	2.13	14
ST_6	VIVO17	trachyte	III	2.40	-	-	7	1.19	n.d.
ST_7	ABB1	trachyte	I-II	2.27	2.63	13.7	13	1.66	33
ST_7	ABB2	trachyte	I-II	2.31	2.59	10.7	4	1.13	35
ST_7	VIVO23	trachyte	I	2.23	2.61	14.6	3	1.02	38
ST_7	VIVO24	trachyte	I	2.27	2.53	10.3	3	1.18	-

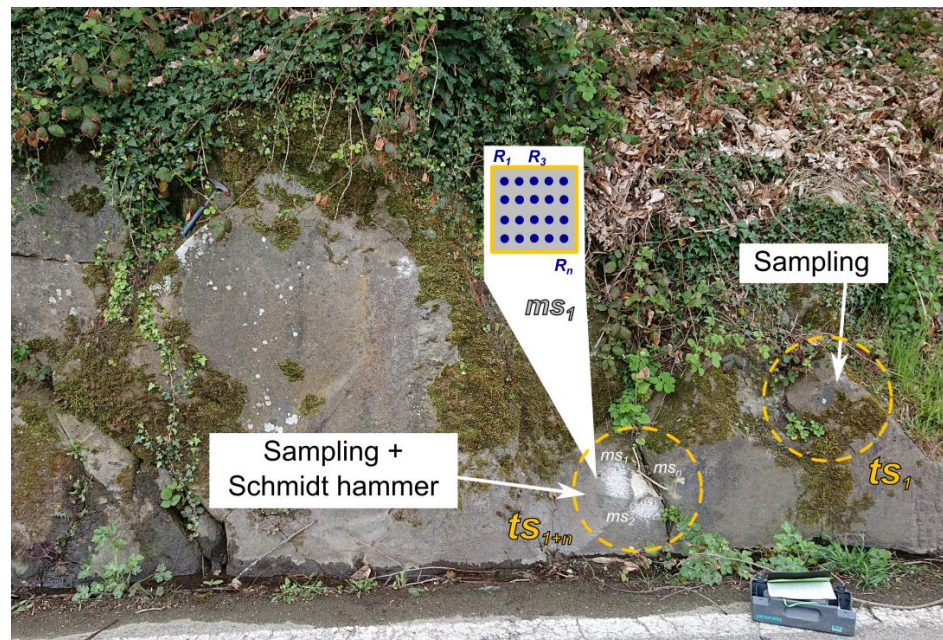


Figure 3. Example of one investigated outcrop and distribution of test sites ts where one or more samples for laboratory determinations are collected. For some ts , a set of k measuring surfaces ms_k ($k \cong 3-6$) is chosen, where we acquire Schmidt hammer rebounds R according to [53]. After fieldwork, for those ts where Schmidt hammer measurements are available, the horizontal rebounds R_h and the ts average rebound \overline{R}_h are calculated.

We characterized all samples in the laboratory for dry density (ρ_d), petrographic characteristics, two-dimensional porosity (n_{2D} , as explained below in the text) and thermal analyses outputs. Instead, we determined the specific gravity of solids (G_s) and porosity (n) for a subset of representative samples.

We implemented the procedure recommended by [54] for the determination of ρ_d , and by [55] for G_s , respectively. These parameters allowed us to calculate n by the following equation [56], where ρ_w is the density of water:

$$n = 1 - [\rho_d / (G_s \rho_w)].$$

In this paper, a method is defined and used to determine a two-dimensional rock void space (from now on 2D porosity n_{2D}) based on image analysis, as previously tested by other authors [57–59]. A polished thin section was prepared from each sample and analysed using a scanning electron microscope (SEM) Philips XL30, operating at 20 kV equipped with a microanalytical energy dispersive system (EDS) EDAX-DX4 (University of Siena). A total of fifteen back-scattered electron (BSE) images were obtained on each section. All images were taken with 8-bit radiometric resolution at the same enlargement value of $35\times$ so that the total surveyed area was always ca. 8 mm^2 . Considering grain and void sizes, we estimated this area as representative of the whole sample. In the BSE images, the “darker” pixels (i.e., those pixels characterized by low digital number DN) represent voids, hence a representative threshold DN (DN_t) must be chosen to perform the binarization of the image and to estimate the void extent. With this aim, we observed that the DN frequency histogram of the BSE images is bimodal and the DN around the secondary mode located toward the lower DN values represent the rock voids (Figure 4a). Hence, we assume the DN_t to be placed between the two modal values, at the DN frequency minimum [60]. This condition is also represented by a nil value of the 1st derivative of the DN frequency histogram (Figure 4b). Having defined DN_t , the void area within the BSE images is represented by the cumulative frequency of pixels with $DN \leq DN_t$ ($f_{<DN_t}$), hence the 2D porosity n_{2D} may be calculated as:

$$n_{2D} = (f_{<DN_t} / f_{tot}) \cdot 100$$

where f_{tot} is the total number of pixels of the image under analysis.

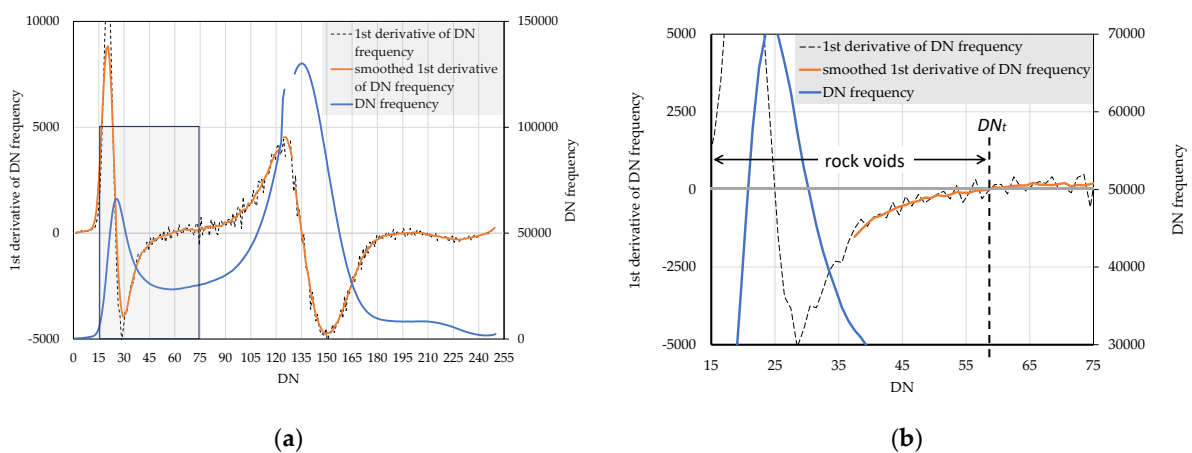


Figure 4. (a) DN frequency distribution of a BSE-SEM image of a representative rock sample under study and corresponding 1st derivative; the DN values around the secondary mode ($DN \cong 28$) correspond to the “darker” pixels representing the rock voids, while the DN values around the primary mode ($DN \cong 135$) are the rock solids. (b) The threshold DN_t , which allows us to separate voids from solids, is assumed to be located where the DN frequency between the modes gets to its minimum (Figure 4a), i.e., the 1st derivative of the DN frequency is nil; these conditions are verified for $DN_t \cong 58$, hence rock voids are represented by $DN \leq 58$.

Standard petrographic descriptions under a polarizing microscope were carried out. Detailed petrographic analyses coupled with chemical characterization of magmatic and secondary minerals were carried out using SEM-EDS.

Thermal analysis (thermogravimetry, TG; differential thermogravimetry, DTG; differential thermal analysis, DTA) were carried out by a simultaneous differential thermal analysis (SDTA) Q600 Thermal-TA Universal instrument (University of Siena). Data were collected in air atmosphere with a flow rate of 20 mL/min, 20 to 900 °C temperature range, and heating rate of 10 °C/min. Analyses were carried out on about 25 mg fine powdered sample in open alumina crucibles. Instrumental theoretical T precision is ± 0.5 °C and theoretical weight sensitivity down to 0.1 μ gr [61].

4. Results

We chose a total of seven outcrops located in the surrounding of the Rifugio Amiantino and Vivo d'Orcia village (north-eastern Monte Amiata, Figure 1). For each outcrop, we collected at least two samples representative of different test sites (*ts*), for a total number of twenty-four samples.

Outcrop and test site information, lithology descriptions and results of analyses performed are summarized in Table 1.

4.1. Engineering Geological Characterization

The average horizontal rebound values \overline{R}_h for the analysed test sites vary from 14 to 44. Significant variation may occur also among test sites of a single outcrop, as can be noticed at Vivo d'Orcia or at the sports ground outcrop (ST_1, ST_2). Considering the visual weathering grade G [25], the \overline{R}_h seems to not vary accordingly. Excluding pumices, where the Schmidt hammer test cannot be carried out given the very low consistence of these rocks, Grade I samples show \overline{R}_h varying from ca. 19 to 44, which also represent the minimum and maximum values registered. Samples of Grade III are related to corestones in saprolite, and they either show the lowest \overline{R}_h value (VIVO16) or do not allow us to perform the Schmidt hammer test due to weathering effects which reduced the rock cohesion.

The pumices from the outcrop ST_2 (Vivo d'Orcia sports ground) show both the lowest ρ_d and the highest n values; moreover, no rebounds and estimates of \overline{R}_h can be obtained. The range of n for trachydacitic lava flows is quite large (1–17%), with no evident correlation with weathering grade. Grade I rocks can show both low ρ_d values associated with high n and the opposite.

The 2D porosity values n_{2D} are quite variable. Voids can be open fractures or vesicles, sometimes elongated and parallel oriented. Massive rocks such as VIVO2 show the lowest values (0.5%), while pumices such as VIVO5 show the highest values (52%). The other high n_{2D} values correspond to other pumices (VIVO4 with 35% and VIVO21 with 20%). n_{2D} values in lava flows range from 0.5% to 22%. Samples with different n_{2D} may have been collected from the same outcrop, testifying that lithological texture is variable at the local scale.

4.2. Petrography

The lava flow samples show a porphyritic texture (Figure 5) with a glassy to perlitic (Figure 5a–c) groundmass, sometimes displaying flow banding structures. Phenocrysts are often broken; zoned plagioclase and sanidine are the most abundant phenocrysts (Figure 5a) followed by orthopyroxenes, biotite (Figure 5a–c) and rare clinopyroxenes. Resorbed quartz crystals occur, and rare mafic aggregates can also be found. All the studied samples often show open or filled fractures and vesicles (Figure 5d). Their abundance varies and this will be discussed in the following section, where the void percentage has been evaluated using an image analysis software. Pumices (Figure 5b) cropping out at ST_2 stop (sports ground) show the same mineralogy of lava flows and a strong flow-like texture of the glassy groundmass. Vesicles are large (up to 1 mm in diameter or length), abundant (Table 1) and parallel oriented.

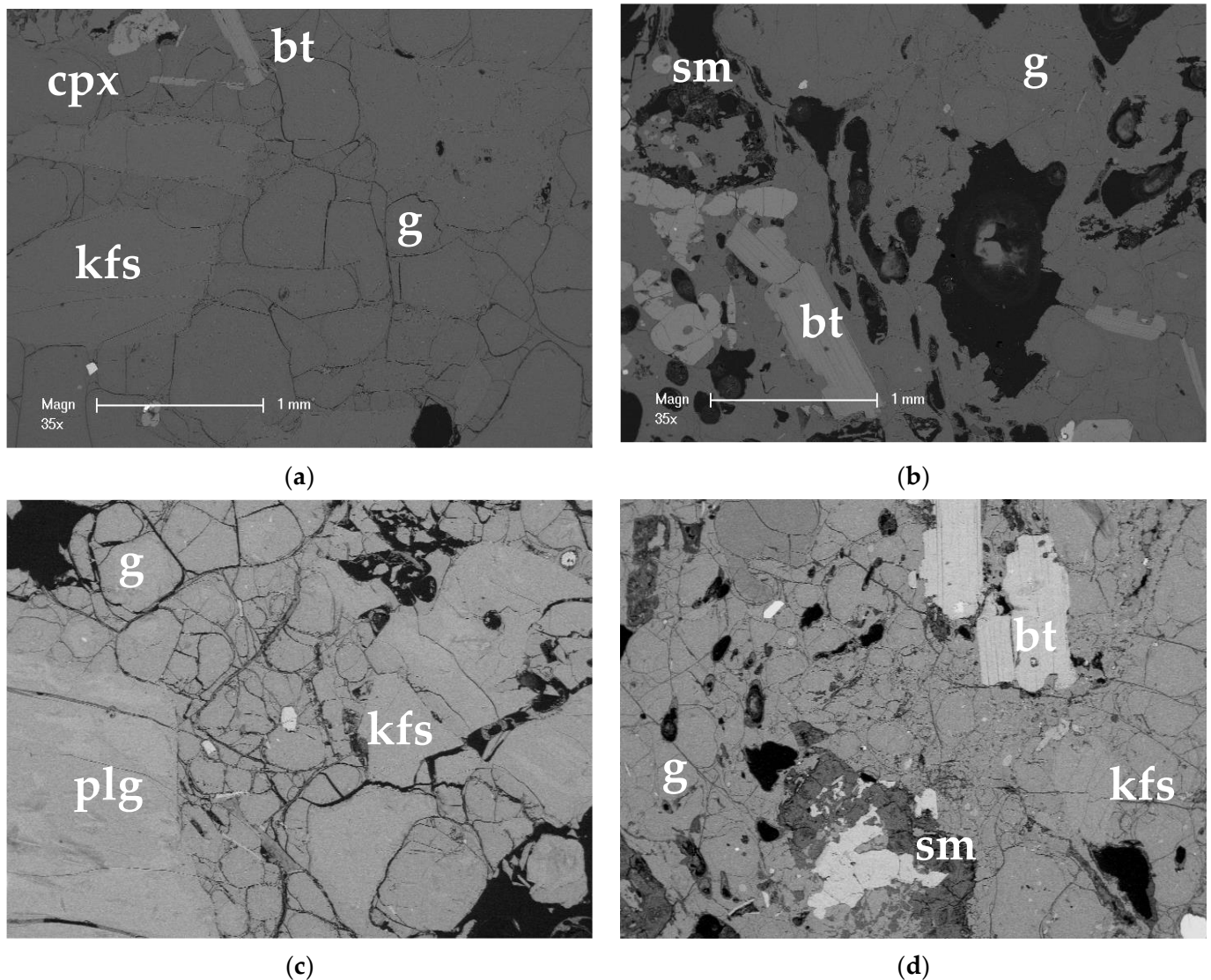


Figure 5. BSE-SEM images of four representative samples: (a) sample VIVO1, from ST_1, showing unweathered perlitic glass (g) and sanidine (kfs) and biotite (bt) phenocrysts; (b) sample VIVO4 (pumice) from ST_2, showing large, elongated vesicles, unweathered biotite phenocrysts and small areas where clay minerals (sm) grow; (c) sample VIVO11 from ST_4, showing a network of fractures filled with clay minerals; glass is still unweathered; (d) sample VIVO16 (ST_6) showing weathered glass and phenocrysts, vesicles and fractures filled with clay minerals.

A detailed study of mineral chemistry of collected samples has not been carried out since previous studies [34,39,40] are exhaustive, and it is not the aim of this research. However, we characterized secondary minerals formed after the glassy groundmass and filling fractures and vesicles in selected samples. We chose one sample for each outcrop. At the ST_2 outcrop, we selected two samples since pumices and lava flows were recognized. When possible, we chose samples where all the engineering geological data were available, so that the dataset was as complete as possible.

Figure 5a,b illustrates how samples collected near the Vivo d’Orcia village (outcrops ST_1 and ST_2), including pumices, are mainly unaltered with fresh glass and unweathered phenocrysts. However, secondary minerals can seldom form in open voids, and their chemical analyses are reported in Table 2. Trachytes from outcrop ST_3 and ST_4 (Figure 5c) show perlitic glass groundmass, open fractures, and voids where secondary minerals grow. Samples from outcrop ST_5 show parallel oriented vesicles and secondary minerals growing along fractures. SEM-BSE images (Figure 5d) for trachytes from out-

crops ST_6 and ST_7 evidence a higher degree of vesicularity with respect to the previous samples, devitrified glass and wide patches of secondary minerals, mainly in the outcrop ST_6 sample.

Table 2. Representative chemical analyses of clay minerals expressed in oxides %, as resulted from EDS spot analyses. Symbol: (-) measurement below the limit of detection.

ID Sample	SiO ₂	Al ₂ O ₃	MgO	FeO	CaO	Na ₂ O	K ₂ O	Na ₂ O + K ₂ O	FeO + MgO
VIVO1	55.82	27.64	0.23	14.32	1.22	0.33	0.44	1.99	14.55
VIVO1	58.95	23.70	0.39	15.15	1.40	0.12	0.30	1.82	15.53
VIVO1	59.46	29.06	0.33	9.31	1.22	0.31	0.30	1.84	9.64
VIVO4	56.50	37.39	0.08	4.46	0.78	0.30	0.50	0.50	4.54
VIVO4	54.63	40.35	0.24	4.11	0.26	0.15	0.26	0.26	4.35
VIVO4	59.23	32.84	0.74	5.61	0.81	0.35	0.42	0.42	6.35
VIVO7	51.28	43.26	0.31	3.64	0.47	0.41	0.62	1.51	3.94
VIVO7	53.04	42.39	0.03	3.41	0.55	0.24	0.35	1.13	3.44
VIVO7	77.55	13.19	0.00	0.37	2.15	2.76	3.99	8.90	0.37
VIVO7	78.81	12.97	0.00	0.37	3.30	3.34	1.20	7.84	0.37
VIVO13	51.33	46.52	0.27	0.43	0.42	0.42	0.61	1.45	0.70
VIVO13	50.68	47.68	0.22	0.60	0.55	0.16	0.11	0.82	0.81
VIVO13	49.72	47.42	0.25	0.57	0.95	0.44	0.64	2.03	0.82
ABB1	83.29	9.06	0.00	0.11	0.40	0.70	6.44	7.54	0.11
ABB1	84.92	8.56	0.00	0.13	0.30	0.54	5.54	6.38	0.13
ABB1	85.74	7.84	0.00	0.08	0.20	0.60	5.54	6.34	0.08
VIVO16	52.44	45.87	-	-	1.69	-	-	1.69	0.00
VIVO16	52.08	46.04	-	-	1.88	-	-	1.88	0.00
VIVO16	59.11	26.62	-	2.91	1.84	1.12	7.61	10.57	2.91
VIVO16	57.98	31.69	-	1.68	-	0.79	7.87	8.66	1.68
VIVO1	55.82	27.64	0.23	14.32	1.22	0.33	0.44	1.99	14.55
VIVO1	58.95	23.70	0.39	15.15	1.40	0.12	0.30	1.82	15.53
VIVO1	59.46	29.06	0.33	9.31	1.22	0.31	0.30	1.84	9.64

Table 2 reports representative chemical analyses of secondary clay minerals in the selected samples. Figure 6 (binary diagrams) illustrates their compositional variation which is not correlated with the weathering grade as defined in Table 1. Trioctahedral-like smectitic composition occurs in most samples except for sample ABB1 from outcrop ST_7 where dioctahedral-like smectites occur. Two compositionally different groups of smectites (alkali-rich and Fe-rich) occur in sample VIVO7 (ST_3). Secondary minerals in VIVO13 show a kaolinite-like composition. Submicrometric dimension and a hollow-like structure (Figure 7a) suggest that it consists of halloysite, the hydrous, low-crystalline phase of kaolinite. Kaolinite-like clays also occur in VIVO16 (ST_6) along with alkali-rich smectites (Figure 7b). Clay minerals can form at the cores or along cleavage planes of phenocrysts (Figure 7c). They can line fractures or grow in fibro-radial to spherulitic masses filling vesicles and secondary voids (Figure 7d). Compositionally different secondary minerals form regardless of different microtextural sites. As an example, in sample VIVO7, the alkali-rich and (Fe + Mg)-rich smectites occur both in vesicles and in fractures indicating no microtextural control on secondary mineral growth. Analogous observation can be made for sample VIVO16, where kaolinite-like and smectite-like compositions occur in fractures and vesicles, indifferently.

4.3. TG, DTG and DTA Data

The main results of thermal analyses are summarized in Table 1. TG, DTG and DTA curves for two representative samples are reported in Figure 8.

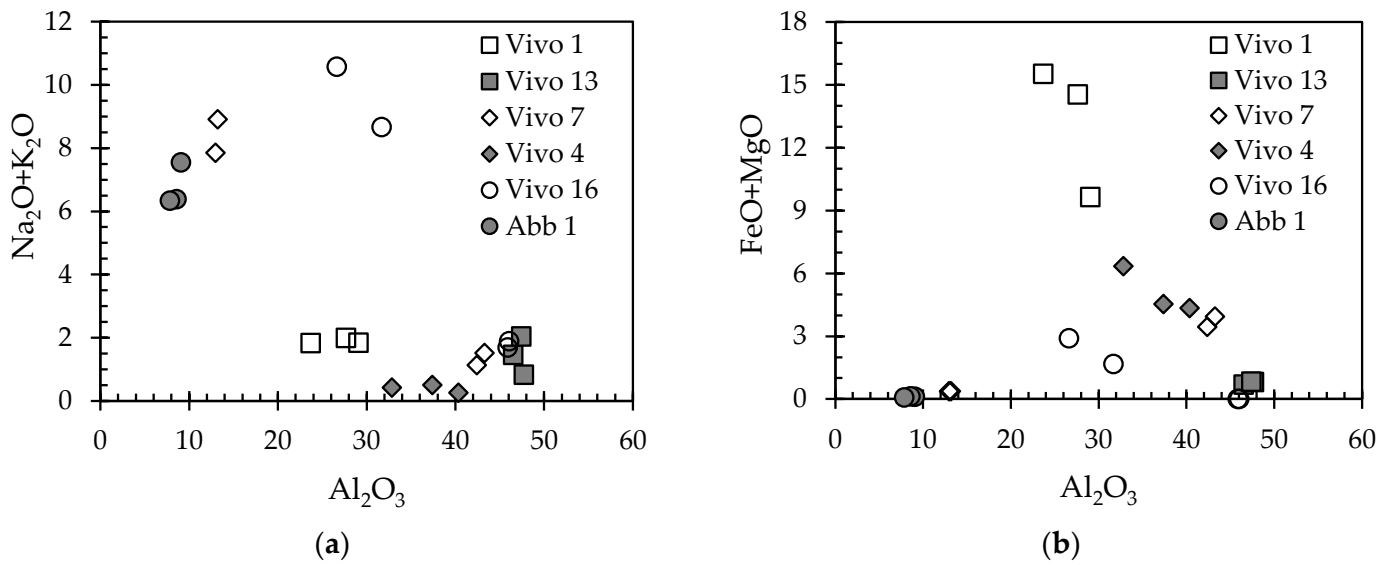


Figure 6. Binary diagrams illustrating variations in clay mineral chemical composition as resulted from SEM-EDS analyses (see Table 2). (a) $\text{Na}_2\text{O} + \text{K}_2\text{O}$ (alkali) versus Al_2O_3 ; (b) $\text{MgO} + \text{FeO}$ versus Al_2O_3 . Two groups of smectites can be recognized. See text for comments.

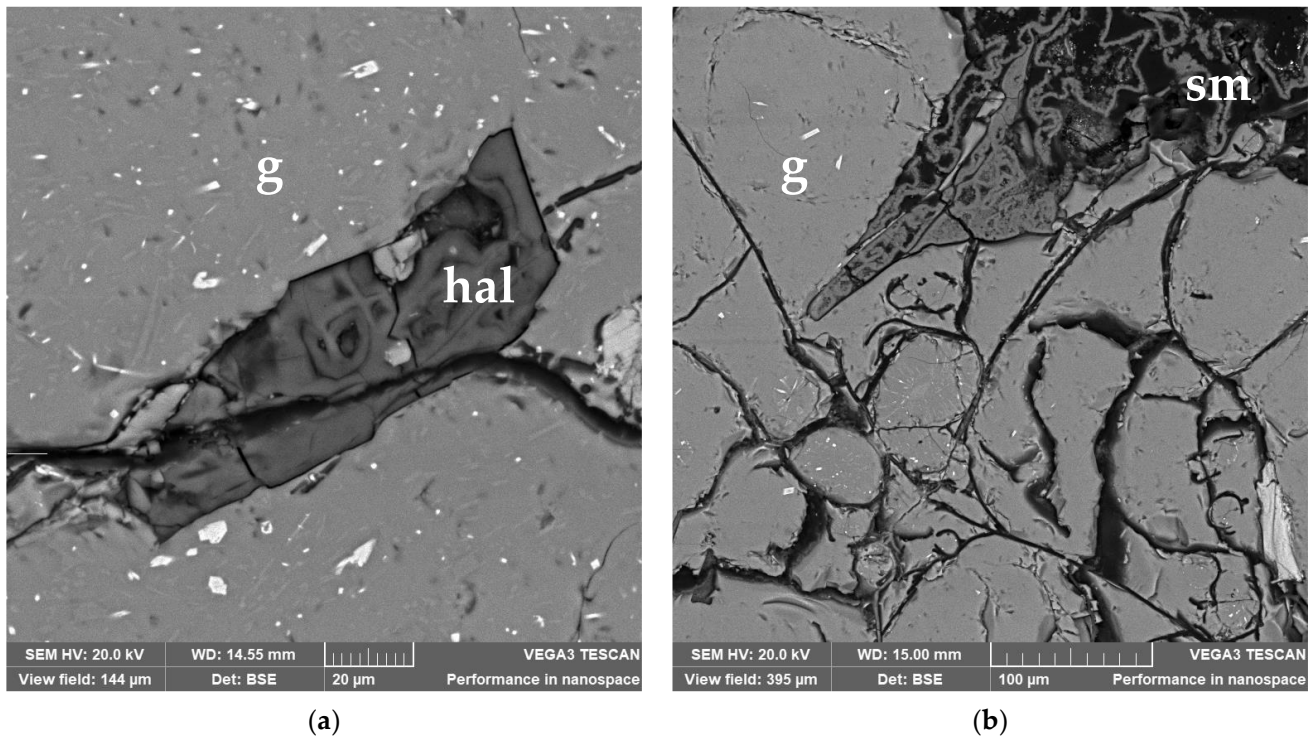


Figure 7. Cont.

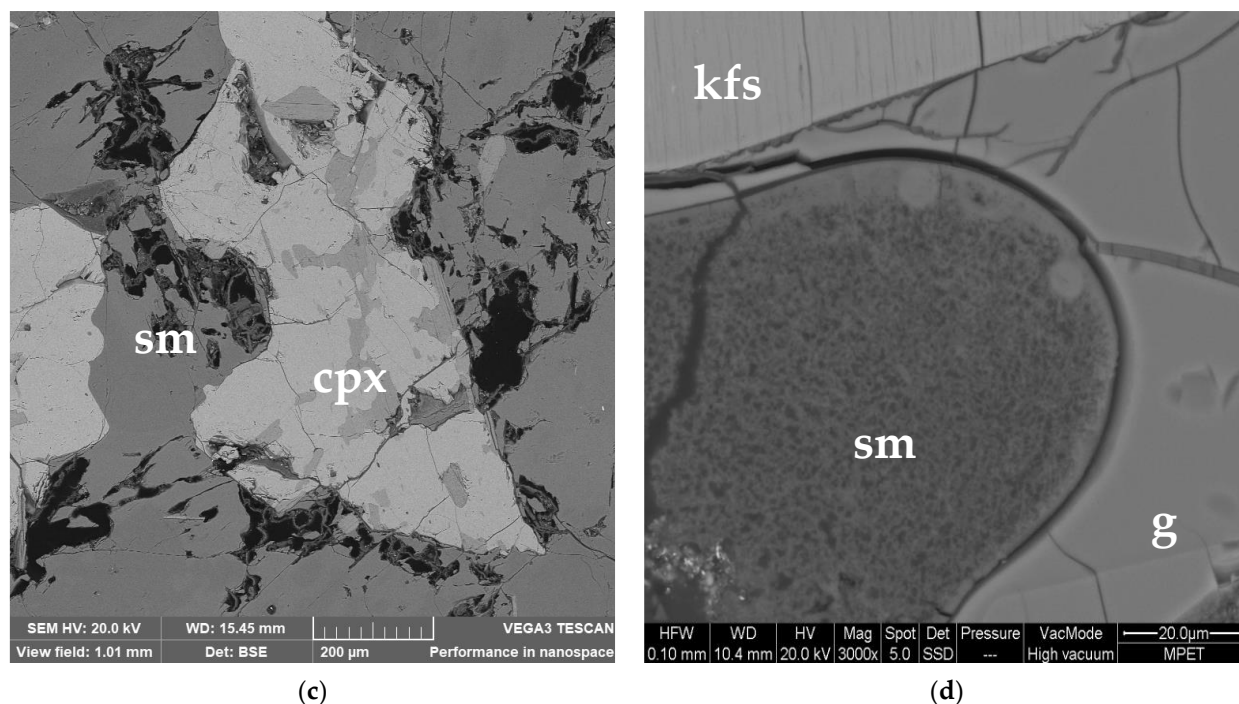
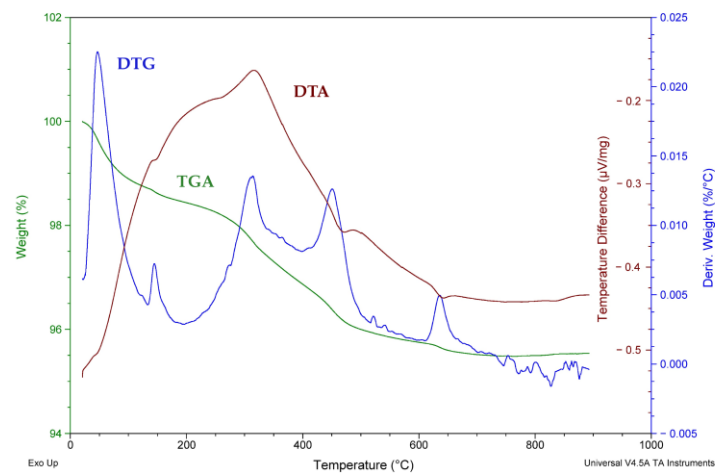


Figure 7. BSE-SEM images illustrating clay minerals: (a) hollow of halloysite (hal) in sample VIVO13 from ST_5; (b) smectites (sm) growing in vesicles in sample VIVO7 from ST_3; (c) smectites in vesicles and on phenocrysts (pyroxene, cpx) in sample VIVO4 from ST_2; (d) spherulitic masses of smectites filling voids in glass (g) (sample VIVO16; ST_6). Kfs: sanidine.

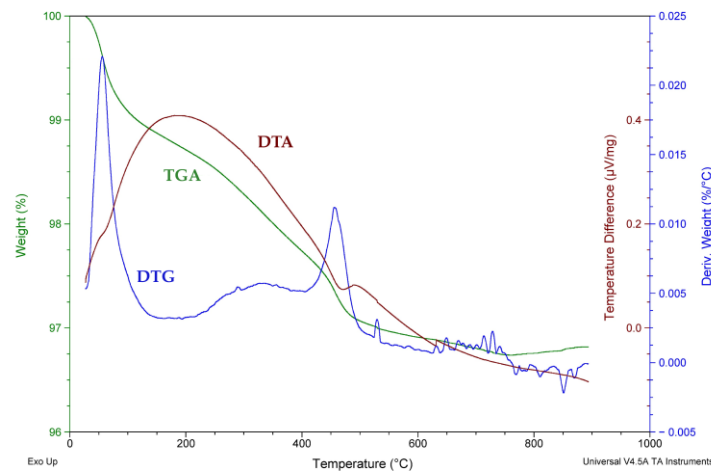
All the curves share some general features. The observed reactions during heating are both endothermic and exothermic. A first reaction always occurs below 100 °C, and it corresponds to a limited weight loss (<2 wt%) due to adsorbed water loss (dehydration). Minor exothermic reactions may occur around 300 °C and are probably correlated to redox reactions. Endothermic reactions have their peaks in the DTA curve between 268 and 475 °C, and they correspond to the main weight loss ranging from 0.85 to 2.79 wt%. Based on previous studies [62–64], the endothermic reactions correspond to dehydroxylation reactions which affect hydrous clay minerals such as smectites and halloysite, the hydrate phase of kaolinite. Temperatures of dehydroxylation of these clay minerals are not strictly constrained. This variability in temperature values results from disorder of the clay mineral structures and strongly varying mineral composition. As an example, the increase in Fe content lowers the dehydroxylation and decomposition temperatures, compared to Al-rich clay minerals [62,65,66].

The SEM-EDS analyses have evidenced that submicroscopic phases formed after glass and in open fractures and vesicles. A stoichiometric composition has not been obtained since these secondary phases result from a clay mineral mixture, probably smectites and halloysite. The TGA curve shapes are gentle, and they do not show sharp peaks. This is evidence of a low-crystallinity material and an extremely variable composition at the micron scale so that the dehydroxylation reactions occur in a temperature range rather than at one defined T°. The only other hydrous phase present in the studied sample is biotite, which is not affected by heating in the investigated temperature range. Exothermic reactions due to recrystallization are not observed.

Following what was previously stated, we can hypothesize that weight loss at the observed higher temperatures (Figure 8) is directly proportional to the secondary clay mineral content in the analysed samples.



(a)



(b)

Figure 8. Thermal analyses results for two representative samples; TGA: thermal gravimetric analysis, DTG: derivative thermogravimetric analysis, DTA: differential thermal analysis. Exothermal signals are up. (a) VIVO7 samples from ST_3; the main weight loss (wt%) occurs between 200 and 500 °C; (b) VIVO22 sample from ST_3; the main weight loss (VIVO7: 2.72 wt%; VIVO22: 1.85 wt%) occurs between 200 and 500 °C.

5. Discussion

The present study has been carried out to investigate the changes in engineering geological properties of trachites and pumices in relation to weathering intensity.

Heterogeneity in geological and mechanical properties has been observed in different parent material with different weathering degrees [4]. Our investigation focusses on compositionally homogeneous (trachydacites) parent material with different weathering degrees.

Variations in rebound values, as resulted from Schmidt hammer measurements, are indicative of deterioration of uniaxial compressive strength (UCS; [15,23,67]). $\overline{R_h}$ has been compared to engineering geological properties such as dry density (ρ_d), specific gravity of solids (G_s) and porosity (n). These properties have also been compared to petrographic characteristics, such as 2D porosity (n_{2D}), as well as weathering grade quantitatively estimated by means of thermal analysis.

Figure 9 illustrates the results of this comparison and, specifically, the significant trends which link the different parameters.

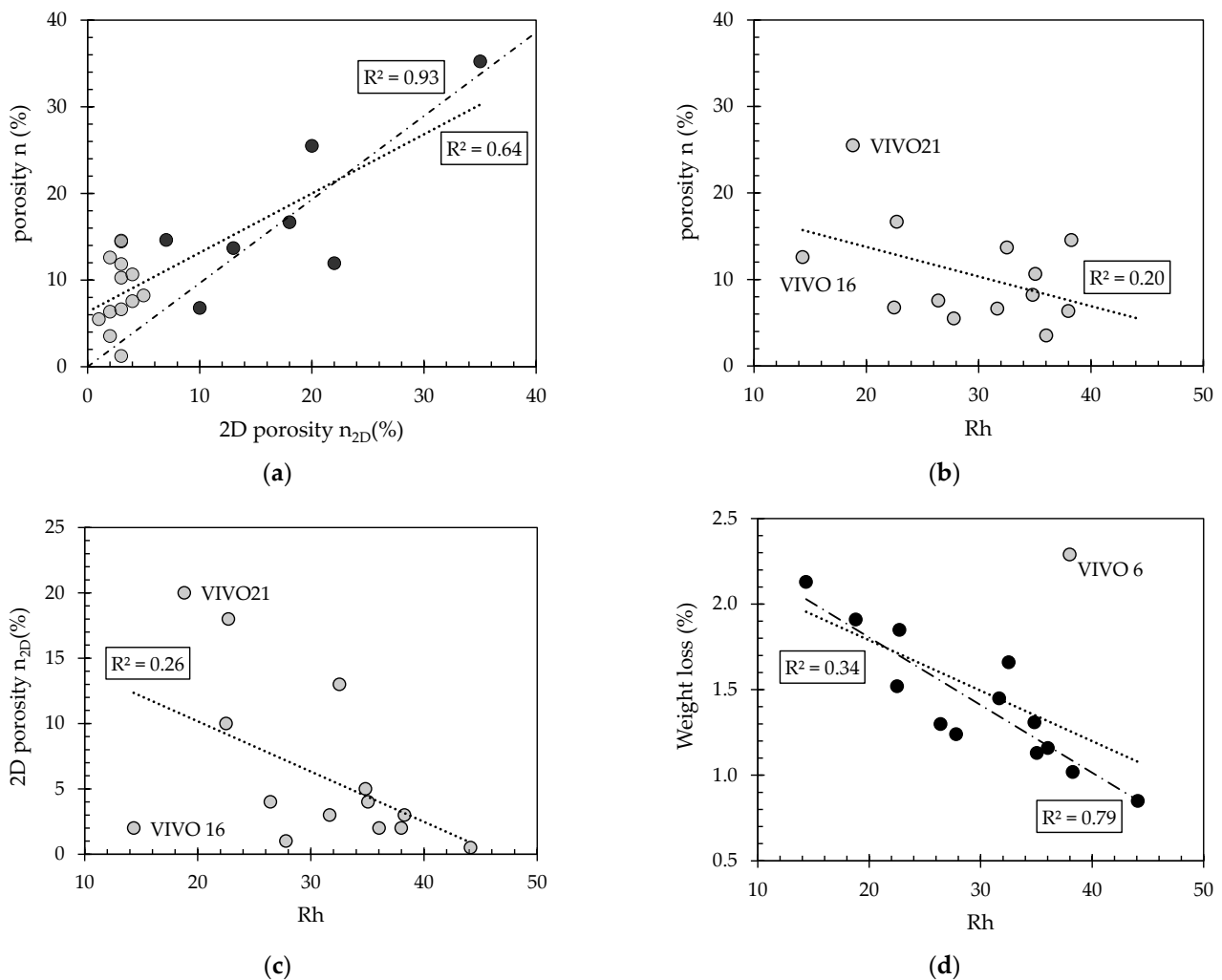


Figure 9. Scatterplots showing relationships among different engineering geological and petrographic properties and corresponding best fit linear trends. The dotted line corresponds to the linear trend obtained from the whole dataset (grey circles and black circles), and the line-point function from the partial dataset (black circles). (a) Porosity n versus 2D porosity n_{2D} ; (b) porosity n versus \bar{R}_h ; (c) 2D porosity n_{2D} versus \bar{R}_h ; (d) weight loss versus \bar{R}_h . See the text for symbols and comments.

Firstly, n is directly correlated with 2D porosity n_{2D} showing an R^2 value of 0.64 (Figure 9a). The analysis of the scatterplot reveals that n is often higher than n_{2D} for the same samples. This condition is systematic and more relevant for $n_{2D} < 6\%$, while almost negligible for $n_{2D} \geq 10\%$. Indeed, the linear trend fitting porosity data for $n_{2D} > 6\%$ (black circles in Figure 9a) are almost close to the bisector with intercept $n < 5\%$; the R^2 value for these data rises to 0.93. The above results may have different reasons. Firstly, especially when rock porosity is low, voids with size of the same order of the thin section thickness, or smaller, may be recorded as “bright” image pixels (i.e., pixels with $DN > DN_i$) because these voids do not involve the whole section thickness. When both voids size and porosity increase, the weight of microscopic voids on n_{2D} determination reduces, so n and n_{2D} tend to assume similar values. Another explanation may lie in the fact that the micrometric vesicles of lava flows are often elongated and parallel oriented, while thin sections used to acquire the BSE images have been cut almost normal to the flow direction; this condition may cause an underestimation of both the void area and n_{2D} . The analysis of further thin

sections differently oriented with respect to the lava flow could help to test this hypothesis, even though this is not within the objectives of this research. Finally, the method here proposed to define the DN_i from the image histogram may affect the n_{2D} values. We highlight that, especially for $n_{2D} > ca. 5\%$, the image-based method to estimate the rock porosity may represent a straightforward tool to perform (at least) first-order porosity estimations by using thin section.

\overline{R}_h values slightly decrease with n and n_{2D} . Many authors [24,28,49,68] have established that UCS generally decreases with increasing porosity. Considering that P and S wave velocity are correlated with UCS, Ref. [28] illustrated that P wave velocity shows an exponential relation with porosity. Conversely, S wave velocity does not show a good correlation. They interpreted this lack of correlation as being due to differences in pore network arrangement, that is the abundance and orientation of small cracks or microfractures. Moreover, a reduction in porosity is related to hydrothermal processes, as pores and cracks can be filled by clay minerals or amorphous silica [28]. Sousa et al. [68] observed low correlation coefficients between UCS and P wave velocity versus crack density in granites. This may be due to them not considering other textural characteristics such as size and preferential crack orientation. Yagiz [49] investigated the relationships between Schmidt hammer tests and UCS and various mechanical properties including effective porosity in different rock types. Effective porosity has a low influence on hardness, which means that significant differences in hardness values correspond to small variations in porosity values. Our results are consistent with the quoted papers. A broad negative correlation exists between \overline{R}_h values and n (Figure 9b,c). This feature suggests that the micrometric and millimetric porosity slightly influences the rock strength. In particular, pumice (VIVO21) with high n (and n_{2D}) shows an intermediate \overline{R}_h value in the dataset, whereas the lowest \overline{R}_h value has been measured on a trachyte sample (VIVO16) with intermediate n and low n_{2D} . Following previous interpretations, we can suggest that a strong correlation between \overline{R}_h and porosity is not always strictly predictable since type, size and distribution of cracks and pores should be considered.

The variation in \overline{R}_h is primarily due to other factors. As evidenced by Figure 9d, \overline{R}_h is directly correlated with the main weight loss percentage obtained from thermal analysis. This loss is due to the presence of hydrous clay minerals, mainly smectites and halloysite, which derive from the weathering of glass and volcanic mineral phases. The higher the amount of these phases that were decomposed during heating, the higher the weight loss registered. VIVO6 plots out of the general negative trend, showing high \overline{R}_h compared with high weight loss (i.e., clay content). Hence, considering the entire set of samples, the correlation between \overline{R}_h and weight loss is low ($R^2 = 0.34$). On the other hand, if we consider VIVO6 as an outlier, the R^2 value strongly increases up to 0.79. We can conclude that the Schmidt hammer rebound, i.e., the rock UCS [23,32], is strictly influenced by the weathering grade as quantitatively estimated by thermal analysis. The data also show that small variations in weathering degree determined by weight losses highly affect the mechanical properties of the investigated volcanic rocks.

6. Conclusions

In this paper, we have illustrated that thermal analysis is a smart method for estimating weathering, simply quantifying the weight loss due to secondary clay mineral abundance. This laboratory index shows a negative linear correlation with Schmidt hammer rebound field measurements, demonstrating that the deterioration of rebound, and in turn of UCS, is related to increasing weathering intensity. In addition, small variations in this weathering-related index imply significant rebound changes. This high sensitivity of a rock mechanical property to secondary mineral content variations means it is worth further investigation. Quartz-feldspathic clastic and magmatic rocks characterized by chemical weathering processes like the investigated trachydacites may represent ideal targets for additional research.

Author Contributions: Conceptualization, L.D., E.D. and G.G.; methodology, L.D., E.D. and G.G.; software, E.D. and G.G.; validation, L.D., E.D., G.G. and C.M.; formal analysis, L.D. and E.D.; investigation, E.D., G.G., L.D. and C.M.; resources, L.D.; data curation, E.D. and G.G.; writing—original draft preparation, E.D., G.G. and L.D.; writing—review and editing, L.D., E.D., G.G. and C.M.; visualization, G.G. and C.M.; supervision, L.D.; project administration, L.D.; funding acquisition, L.D. All authors have read and agreed to the published version of the manuscript.

Funding: Dipartimento di Scienze Fisiche, della Terra e dell’Ambiente within the project “Accordo di collaborazione scientifica tra Unione Comuni Amiata-Val d’Orcia e Università di Siena (coord.: L. Disperati): 6100.

Data Availability Statement: All data generated or analysed for this study are included in this article, and the related datasets may be available from the corresponding author upon request.

Acknowledgments: The authors wish to thank Daniele Rappuoli and Fabrizio Piccinelli of Unione dei Comuni Amiata-Val d’Orcia and Nicola Prezzolini of Comune di Abbadia S. Salvatore for logistic support during fieldwork. We are deeply grateful to the three anonymous reviewers who contributed greatly to the improvement of the manuscript.

Conflicts of Interest: The authors declare no conflict of interest.

References

1. Barton, N.; Choubey, V. The Shear Strength of Rock Joints in Theory and Practice. *Rock Mech. Felsmech. Mécanique Roches* **1977**, *10*, 1–54. [[CrossRef](#)]
2. Barton, N. The Shear Strength of Rock and Rock Joints. *Int. J. Rock Mech. Min. Sci.* **1976**, *13*, 255–279. [[CrossRef](#)]
3. Hoek, E.; Brown, E.T. Practical Estimates of Rock Mass Strength. *Int. J. Rock Mech. Min. Sci.* **1997**, *34*, 1165–1186. [[CrossRef](#)]
4. Okewale, I.A.; Grobler, H. Inherent Complexities in Weathered Rocks: A Case of Volcanic Rocks. *Rock Mech. Rock Eng.* **2021**, *54*, 5533–5554. [[CrossRef](#)]
5. Dixon, J.L.; Heimsath, A.M.; Amundson, R. The Critical Role of Climate and Saprolite Weathering in Landscape Evolution. *Earth Surf. Process. Landforms* **2009**, *34*, 1507–1521. [[CrossRef](#)]
6. Migoñ, P. Mass Movement and Landscape Evolution in Weathered Granite and Gneiss Terrains. *Geol. Soc. Lond. Eng. Geol. Spec. Publ.* **2010**, *23*, 33–45. [[CrossRef](#)]
7. Hack, R.; Price, D.; Rengers, N. A New Approach to Rock Slope Stability—A Probability Classification (SSPC). *Bull. Eng. Geol. Environ.* **2003**, 167–184. [[CrossRef](#)]
8. Pantelidis, L. Rock Slope Stability Assessment through Rock Mass Classification Systems. *Int. J. Rock Mech. Min. Sci.* **2009**, *46*, 315–325. [[CrossRef](#)]
9. Durgin, P.B. Landslides and the Weathering of Granitic Rocks. *GSA Rev. Eng. Geol.* **1977**, *3*, 125–131. [[CrossRef](#)]
10. Borrelli, L.; Greco, R.; Gullà, G. Weathering Grade of Rock Masses as a Predisposing Factor to Slope Instabilities: Reconnaissance and Control Procedures. *Geomorphology* **2007**, *87*, 158–175. [[CrossRef](#)]
11. Langella, A.; Di Benedetto, C.; Calcaterra, D.; Cappelletti, P.; D’Amore, M.; Di Martire, D.; Graziano, S.F.; Papa, L.; Langella, A. The Neapolitan Yellow Tuff: An Outstanding Example of Heterogeneity. *Constr. Build. Mater.* **2017**, *136*, 361–373. [[CrossRef](#)]
12. Calcaterra, D.; Parise, M. Weathering in the Crystalline Rocks of Calabria, Italy, and Relationships to Landslides. *Geol. Soc. Eng. Geol. Spec. Publ.* **2010**, *23*, 105–130. [[CrossRef](#)]
13. Prodan, M.V.; Arbanas, Ž. Analysis of the Possible Reactivation of the Krbavčiči Landslide in Northern Istria, Croatia. *Geosciences* **2020**, *10*, 294. [[CrossRef](#)]
14. Fookes, P.G.; Gourley, C.S.; Ohikere, C. Rock Weathering in Engineering Time. *Q. J. Eng. Geol. Hydrogeol.* **1988**, *21*, 33–57. [[CrossRef](#)]
15. Gupta, A.S.; Seshagiri Rao, K. Weathering Effects on the Strength and Deformational Behaviour of Crystalline Rocks under Uniaxial Compression State. *Eng. Geol.* **2000**, *56*, 257–274. [[CrossRef](#)]
16. Yasir, M.; Ahmed, W.; Islam, I.; Sajid, M.; Janjuhah, H.T.; Kontakiotis, G. Composition, Texture, and Weathering Controls on the Physical and Strength Properties of Selected Intrusive Igneous Rocks from Northern Pakistan. *Geosciences* **2022**, *12*, 273. [[CrossRef](#)]
17. Moye, D.G. Engineering Geology for the Snow Mountain Schema. *J. Inst. Aust.* **1955**, *27*, 281–299.
18. Monticelli, J.P.; Ribeiro, R.; Futai, M. Relationship between Durability Index and Uniaxial Compressive Strength of a Gneissic Rock at Different Weathering Grades. *Bull. Eng. Geol. Environ.* **2020**, *79*, 1381–1397. [[CrossRef](#)]
19. del Potro, R.; Hürlimann, M. The Decrease in the Shear Strength of Volcanic Materials with Argillic Hydrothermal Alteration, Insights from the Summit Region of Teide Stratovolcano, Tenerife. *Eng. Geol.* **2009**, *104*, 135–143. [[CrossRef](#)]
20. Rodríguez-Losada, J.A.; Hernández-Gutiérrez, L.E.; Olalla, C.; Perucho, A.; Serrano, A.; Eff-Darwich, A. Geomechanical Parameters of Intact Rocks and Rock Masses from the Canary Islands: Implications on Their Flank Stability. *J. Volcanol. Geotherm. Res.* **2009**, *182*, 67–75. [[CrossRef](#)]
21. Okewale, I.A.; Coop, M.R. A Study of the Effects of Weathering on Soils Derived from Decomposed Volcanic Rocks. *Eng. Geol.* **2017**, *222*, 53–71. [[CrossRef](#)]

22. Rocchi, I.; Coop, M.R. The Effects of Weathering on the Physical and Mechanical Properties of a Granitic Saprolite. *Geotechnique* **2015**, *65*, 482–493. [[CrossRef](#)]
23. Basu, A.; Celestino, T.B.; Bortolucci, A.A. Evaluation of Rock Mechanical Behaviors under Uniaxial Compression with Reference to Assessed Weathering Grades. *Rock Mech. Rock Eng.* **2009**, *42*, 73–93. [[CrossRef](#)]
24. Pola, A.; Crosta, G.B.; Fusi, N.; Castellanza, R. General Characterization of the Mechanical Behaviour of Different Volcanic Rocks with Respect to Alteration. *Eng. Geol.* **2014**, *169*, 1–13. [[CrossRef](#)]
25. Atkinson, R.H.; Bamford, W.E.; Broch, E.; Deere, D.U.; Franklin, J.A.; Nieble, C.; Rummel, F.; Tarkoy, R.J.; Van Duyse, H. Suggested Methods for Determining Hardness and Abrasiveness of Rocks. *Int. J. Rock Mech. Min. Sci.* **1978**, *15*, 89–97.
26. International Society for Rock Mechanics and Rock Engineering. *Rock Characterization, Testing & Monitoring: ISRM Suggested Methods*; Brown, E.T., Ed.; Pergamon Press: Oxford, UK, 1981.
27. Momeni, A.A.; Khanlari, G.R.; Heidari, M.; Sepahi, A.A.; Bazvand, E. New Engineering Geological Weathering Classifications for Granitoid Rocks. *Eng. Geol.* **2015**, *185*, 43–51. [[CrossRef](#)]
28. Pola, A.; Crosta, G.; Fusi, N.; Barberini, V.; Norini, G. Influence of Alteration on Physical Properties of Volcanic Rocks. *Tectonophysics* **2012**, *566–567*, 67–86. [[CrossRef](#)]
29. Nesbitt, H.; Young, G.M. Early Proterozoic Climates and Plate Motions Inferred from Major Element Chemistry of Lutites. *Nature* **1982**, *299*, 715–717. [[CrossRef](#)]
30. Young, G.M.; Wayne Nesbitt, H. Paleoclimatology and Provenance of the Glaciogenic Gowganda Formation (Paleoproterozoic), Ontario, Canada: A Chemostratigraphic Approach. *Geol. Soc. Am. Bull.* **1999**, *111*, 264–274. [[CrossRef](#)]
31. Zhao, H.; Grasby, S.E.; Wang, X.; Zhang, L.; Liu, Y.; Chen, Z.-Q.; Hu, Z.; Huang, Y. Mercury Enrichments during the Carnian Pluvial Event (Late Triassic) in South China. *Bulletin* **2022**, *134*, 2709–2720.
32. Aydin, A.; Basu, A. The Schmidt Hammer in Rock Material Characterization. *Eng. Geol.* **2005**, *81*, 1–14. [[CrossRef](#)]
33. Köken, E.; Özarlan, A.; Bacak, G. Weathering Effects on Physical Properties and Material Behaviour of Granodiorite Rocks. *Rock Mech. Rock Eng. Past Futur.* **2016**, *1*, 331–336. [[CrossRef](#)]
34. Ferrari, L.; Conticelli, S.; Burlamacchi, L.; Manetti, P. Volcanological Evolution of the Monte Amiata, Southern Tuscany: New Geological and Petrochemical Data. *Acta Vulcanol.* **1996**, *8*, 41–56.
35. Laurenzi, M.A.; La Felice, S. Nuovi Dati Geocronologici Sulle Vulcaniti Incontrate Dal Pozzo David Lazzaretti. In *Vulcano Monte Amiata Esa Ed. Firenze*; Regione Toscana: Florence, Italy, 2017; pp. 233–244.
36. Marroni, M.; Moratti, G.; Costantini, A.; Conticelli, S.; Benvenuti, M.G.; Pandolfi, L.; Bonini, M.; Cornamusini, G.; Laurenzi, M.A. Geology of the Monte Amiata Region, Southern Tuscany, Central Italy. *Ital. J. Geosci.* **2015**, *134*, 171–199. [[CrossRef](#)]
37. Peccerillo, A. Plio-Quaternary Magmatism in Italy. *Episodes* **2003**, *26*, 222–226. [[CrossRef](#)]
38. Brogi, A.; Liotta, D.; Meccheri, M.; Fabbrini, L. Transtensional Shear Zones Controlling Volcanic Eruptions: The Middle Pleistocene Mt Amiata Volcano (Inner Northern Apennines, Italy). *Terra Nov.* **2010**, *22*, 137–146. [[CrossRef](#)]
39. Conticelli, S.; Boari, E.; Burlamacchi, L.; Cifelli, F.; Moscardi, F.; Laurenzi, M.A.; Pedraglio, L.F.; Francalanci, L.; Benvenuti, M.G.; Braschi, E.; et al. Geochemistry and Sr-Nd-Pb Isotopes of Monte Amiata Volcano, Central Italy: Evidence for Magma Mixing between High-K Calc-Alkaline and Leucititic Mantle-Derived Magmas. *Ital. J. Geosci.* **2015**, *134*, 266–290. [[CrossRef](#)]
40. Cadoux, A.; Pinti, D.L. Hybrid Character and Pre-Eruptive Events of Mt Amiata Volcano (Italy) Inferred from Geochronological, Petro-Geochemical and Isotopic Data. *J. Volcanol. Geotherm. Res.* **2009**, *179*, 169–190. [[CrossRef](#)]
41. Principe, C.; Vezzoli, L. Characteristics and Significance of Intravolcanic Saprolite Paleoweathering and Associate Paleosurface in a Silicic Effusive Volcano: The Case Study of Monte Amiata (Middle Pleistocene, Tuscany, Italy). *Geomorphology* **2021**, *392*, 107922. [[CrossRef](#)]
42. Pavich, M.J. Processes and Rates of Saprolite Production and Erosion on a Foliated Granitic Rock of the Virginia Piedmont. *Rates Chem. Weather. Rocks Miner.* **1986**, *2*, 551–590.
43. Deere, D.U.; Patton, F.U. Slope Stability in Residual Soils. In *Proceedings of the 4th Pan-American Conference on Soil Mechanics and Foundation Engineering*; American Society of Civil Engineers: Reston, VA, USA, 1971; pp. 87–170.
44. Aydin, A.; Duzgoren-Aydin, N.S.; Malpas, J.G. A Review of Igneous and Metamorphic Saprolites. *J. Nepal Geol. Soc.* **2000**, *22*, 11–16. [[CrossRef](#)]
45. Deere, D.U.; Miller, R.P. *Engineering Classification and Index Properties for Intact Rock*; Kirtland Air Force Base: Albuquerque, NM, USA; p. 1966.
46. Karaman, K.; Kesimal, A. A Comparative Study of Schmidt Hammer Test Methods for Estimating the Uniaxial Compressive Strength of Rocks. *Bull. Eng. Geol. Environ.* **2015**, *74*, 507–520. [[CrossRef](#)]
47. Armaghani, D.J.; Tonnizam Mohamad, E.; Momeni, E.; Monjezi, M.; Sundaram Narayanasamy, M. Prediction of the Strength and Elasticity Modulus of Granite through an Expert Artificial Neural Network. *Arab. J. Geosci.* **2016**, *9*, 1–16. [[CrossRef](#)]
48. Hebib, R.; Belhai, D.; Alloul, B. Estimation of Uniaxial Compressive Strength of North Algeria Sedimentary Rocks Using Density, Porosity, and Schmidt Hardness. *Arab. J. Geosci.* **2017**, *10*, 1–13. [[CrossRef](#)]
49. Yagiz, S. Predicting Uniaxial Compressive Strength, Modulus of Elasticity and Index Properties of Rocks Using the Schmidt Hammer. *Bull. Eng. Geol. Environ.* **2009**, *68*, 55–63. [[CrossRef](#)]
50. International Society for Rock Mechanics, I. *Suggested Methods for Determining Hardness and Abrasiveness of Rocks*; Elsevier: Amsterdam, The Netherlands, 1978.

51. ASTM. *Standard Test Method for Determination of Rock Hardness by Rebound Hammer Method*; ASTM International: Conshohocken, PA, USA, 2001.
52. Basu, A.; Aydin, A. A Method for Normalization of Schmidt Hammer Rebound Values. *Int. J. Rock Mech. Min. Sci.* **2004**, *41*, 1211–1214. [[CrossRef](#)]
53. Aydin, A. ISRM Suggested Method for Determination of the Schmidt Hammer Rebound Hardness: Revised Version. *Int. J. Rock Mech. Min. Sci.* **2009**, *46*, 627–634. [[CrossRef](#)]
54. International Society for Rock Mechanics and Rock Engineering. *Suggested Methods for Determining Water Content, Porosity, Density Absorption and Related Properties and Swelling and Slake-Durability Index Properties*; International Society for Rock Mechanics and Rock Engineering: Salzburg, Austria, 1977; Volume 16.
55. Germaine, J.T.; Germaine, A.V. *Geotechnical Laboratory Measurements for Engineers*; John Wiley & Sons: Hoboken, NJ, USA, 2009.
56. Terzaghi, K.; Peck, R.B.; Mesri, G. *Soil Mechanics in Engineering Practice*; John Wiley & Sons: Hoboken, NJ, USA, 1996.
57. Iscan, A.G.; Kok, M. V Porosity and Permeability Determinations in Sandstone and Limestone Rocks Using Thin Section Analysis Approach. *Energy Sources Part A Recover. Util. Environ. Eff.* **2009**, *31*, 568–575. [[CrossRef](#)]
58. Pavičić, I.; Briševac, Z.; Vrbaški, A.; Grgasović, T.; Duić, Ž.; Šijak, D.; Dragičević, I. Geometric and Fractal Characterization of Pore Systems in the Upper Triassic Dolomites Based on Image Processing Techniques (Example from Žumberak Mts, NW Croatia). *Sustainability* **2021**, *13*, 7668. [[CrossRef](#)]
59. Datta, D.; Thakur, N.; Ghosh, S.; Poddar, R.; Sengupta, S. Determination of Porosity of Rock Samples from Photomicrographs Using Image Analysis. In Proceedings of the 2016 IEEE 6th International Conference on Advanced Computing (IACC), Bhimavaram, India, 27–28 February 2016; pp. 320–325.
60. Oliveira, E.R.; Disperati, L.; Cenci, L.; Pereira, L.G.; Alves, F.L. Multi-Index Image Differencing Method (MINDED) for Flood Extent Estimations. *Remote Sens.* **2019**, *11*, 1305. [[CrossRef](#)]
61. Viti, C. Serpentine Minerals Discrimination by Thermal Analysis. *Am. Mineral.* **2010**, *95*, 631–638. [[CrossRef](#)]
62. Smykatz-Kloss, W. *Differential Thermal Analysis: Application and Results in Mineralogy*; Springer: Berlin, Germany, 1974.
63. Russell, M.; Parfitt, R.L.; Claridge, G.G.C. Estimation of the Amounts of Allophane and Other Materials in the Clay Fraction of an Egmont Loam Profile and Other Volcanic Ash Soils, New Zealand. *Aust. J. Soil Res.* **1981**, *19*, 185–195. [[CrossRef](#)]
64. Ding, Z.; Frost, R.L. Controlled Rate Thermal Analysis of Nontronite. *Thermochim. Acta* **2002**, *389*, 185–193. [[CrossRef](#)]
65. Bloise, A.; Belluso, E.; Barrese, E.; Miriello, D.; Apollaro, C. Synthesis of Fe-Doped Chrysotile and Characterization of the Resulting Chrysotile Fibers. *Cryst. Res. Technol.* **2009**, *44*, 590–596. [[CrossRef](#)]
66. Viti, C.; Giacobbe, C.; Gualtieri, A.F. Quantitative Determination of Chrysotile in Massive Serpentinities Using DTA: Implications for Asbestos Determinations. *Am. Mineral.* **2011**, *96*, 1003–1011. [[CrossRef](#)]
67. Kumavat, H.R.; Chandak, N.R.; Patil, I.T. Factors Influencing the Performance of Rebound Hammer Used for Non-Destructive Testing of Concrete Members: A Review. *Case Stud. Constr. Mater.* **2021**, *14*, e00491. [[CrossRef](#)]
68. Sousa, L.M.O.; Suárez del Río, L.M.; Calleja, L.; Ruiz de Argandoña, V.G.; Rodríguez Rey, A. Influence of Microfractures and Porosity on the Physico-Mechanical Properties and Weathering of Ornamental Granites. *Eng. Geol.* **2005**, *77*, 153–168. [[CrossRef](#)]

Disclaimer/Publisher’s Note: The statements, opinions and data contained in all publications are solely those of the individual author(s) and contributor(s) and not of MDPI and/or the editor(s). MDPI and/or the editor(s) disclaim responsibility for any injury to people or property resulting from any ideas, methods, instructions or products referred to in the content.